



# Deciphering the microstructural evolution and adiabatic shearing behavior of the titanium alloy with stress-induced $\omega$ phase transformation during dynamic compression



Kai Chen<sup>a</sup>, Qunbo Fan<sup>a,b</sup>, Lin Yang<sup>a,b,\*</sup>, Jiahao Yao<sup>a,b</sup>, Shun Xu<sup>a,b</sup>, Wei Lei<sup>a</sup>, Yu Gao<sup>a</sup>

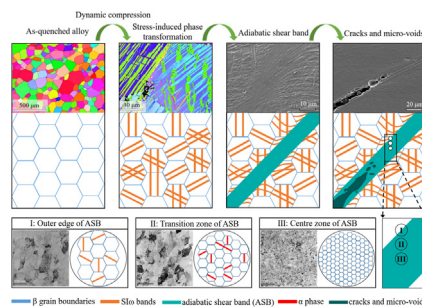
<sup>a</sup> National Key Laboratory of Science and Technology on Materials Under Shock and Impact, School of Materials Science and Engineering, Beijing Institute of Technology, Beijing 100081, China

<sup>b</sup> Beijing Institute of Technology Chongqing Innovation Center, Chongqing 401135, China

## HIGHLIGHTS

- A novel metastable  $\beta$  titanium alloy Ti-6Mo-3.5Cr-1Zr with stress-induced  $\omega$  phase transformation is designed.
- The alloy exhibits strain hardening during dynamic compression because of the stress-induced phase transformation.
- The stress-induced structures hinder the formation and propagation of adiabatic shear bands (ASB).
- The microstructural evolution along outer edge  $\rightarrow$  transition zone  $\rightarrow$  center of the ASB region corresponds to  $(\beta + \omega) \rightarrow (\beta + \alpha) \rightarrow (\beta)$ .

## GRAPHICAL ABSTRACT



## ARTICLE INFO

### Article history:

Received 19 April 2022

Revised 13 June 2022

Accepted 9 July 2022

Available online 12 July 2022

### Keywords:

Titanium alloy

Dynamic compression

Stress-induced  $\omega$  phase transformation

Adiabatic shear band

Microstructural evolution

## ABSTRACT

Metastable  $\beta$  titanium alloys are attracting great interest due to their intricate plastic deformation mechanisms. In this work, a novel metastable  $\beta$  titanium alloy Ti-6Mo-3.5Cr-1Zr is developed by controlling the phase stability. The alloy exhibits a compressive strength of  $\sim 1152$  MPa with large malleability ( $\sim 34\%$ ) during dynamic compressions. The microstructural evolution and adiabatic shearing behavior of the alloy are investigated by applying stop rings to control the compressive strains. Microstructural characterizations and differential scanning calorimetry show that the content of stress-induced  $\omega$  ( $\text{Sl}\omega$ ) phase increases with the accumulation of strain, resulting in strain hardening of the material. The formation of adiabatic shear band (ASB) is observed in samples with 30% strain, whilst the formation and expansion of ASB are hindered by stress-induced structures. The microstructural evolution along outer edge  $\rightarrow$  transition zone  $\rightarrow$  center of the ASB region corresponds to  $(\beta + \omega) \rightarrow (\beta + \alpha) \rightarrow (\beta)$ , which is caused by the temperature increase in ASB. In addition, the average grain sizes in ASB region are gradually refined under the action of dynamic recrystallization. These results provide insights into the dynamic deformation mechanism and adiabatic shearing behavior of metastable  $\beta$  titanium alloys.

© 2022 Published by Elsevier Ltd. This is an open access article under the CC BY-NC-ND license (<http://creativecommons.org/licenses/by-nc-nd/4.0/>).

\* Corresponding author.

E-mail address: [linyang@bit.edu.cn](mailto:linyang@bit.edu.cn) (L. Yang).

## 1. Introduction

Metastable  $\beta$  titanium alloys have broad applications in the fields of aerospace, armored vehicles and biomedicine, due to their high specific strength, high corrosion resistance and low elastic modulus [1–6]. Recently, considerable efforts have been devoted to the development of titanium alloys with high-strength and high-ductility, governed by a variety of deformation mechanisms (such as dislocation slip, stress-induced phase transformation and twinning). d-electrons theory was first proposed by Morinaga [7] to predict the plastic deformation modes of titanium alloys, in which two electronic parameters of Md (the metal d-orbital energy level) and Bo (the covalent bond strength between Ti and an alloying element) were applied to assess the stability of  $\beta$  phase. Based on this theory, a series of metastable  $\beta$  titanium alloys such as Ti-12Mo [8], Ti-9Mo-6W [9], Ti-15Nb-5Zr-4Sn-1Fe [10] and Ti-4Mo-3Cr-1Fe [11] were designed to trigger stress-induced phase transformation and/or stress-induced twinning during the quasi-static deformation. The transformation induced plasticity (TRIP) and twinning induced plasticity (TWIP) effects improve the ductility of these alloys. What's more, due to the hindering effect of the stress-induced structures on dislocations, the materials exhibit an increased strength.

These metastable  $\beta$  titanium alloys break through the long-standing strength-ductility trade-off under quasi-static deformations. However, the deformation and failure mechanisms under dynamic conditions are quite different, one of the most significant differences is the adiabatic shear band (ASB), which appears in titanium alloys due to plastic instability during dynamic compression, causing the adiabatic shear failure [12–14]. Studies through high-speed photography and infrared temperature measurement have shown that the temperature and local strain in the ASB region are much larger than that in the matrix [15,16]. Besides, the high density of geometrically necessary dislocations in ASB is detected by the precession electron diffraction [17]. The adiabatic shearing behavior of a titanium alloy is controlled by its microstructure: in pure titanium containing both coarse and ultrafine grains, the average grain size and texture evolution in the ASB region are significantly affected by the energy stored in the matrix [18]; in Ti-1300 alloy, the  $\alpha + \beta$  lamellar microstructure is more susceptible to adiabatic shear localization deformation than  $\beta$  phase microstructure [19]; in Ti-6Al-4V alloy, the ASBs are found regularly clustering distributed in the bimodal structure, but net-like distributed in the lamellar structure [20]. Different from traditional titanium alloys, the metastable  $\beta$  titanium alloys undergo complex microstructural evolution during the deformation, therefore, it is crucial to investigate the dynamic deformation mechanisms, in order to improve its dynamic mechanical properties and expand its application scope.

Yet, limited researches have been conducted on the dynamic deformation of metastable  $\beta$  titanium alloys. Yang detected the formation of twinning and martensite during dynamic compression of

Ti-8.5Cr-1.5Sn [21], which is similar to the phenomenon that Brozek found in the quasi-static tension test [22]. Xiao [23] analyzed the sequential mechanism of plastic deformation modes activated in Ti-2Al-9.2Mo-2Fe during dynamic compression and the effects of different deformation mechanisms on textures. The twins and martensite were found inside the ASBs of some titanium alloys because of the high temperature and high quenching rate within ASB region [24–27]. Especially, the twinning in ASB were demonstrated to enhance the dynamic recrystallization [28]. These alloys exhibit intricate stress-induced transitions during dynamic deformation, however, the microstructural evolution is difficult to track because of the high-speed characteristic of dynamic deformation. Hence, the effect of stress-induced structures on the adiabatic shearing behavior of alloys is still controversial.

The purpose of this work is to elucidate the mechanisms of the microstructural evolution and adiabatic shearing behavior for metastable  $\beta$  titanium alloys under dynamic deformations. A novel metastable  $\beta$  titanium alloy Ti-6Mo-3.5Cr-1Zr (wt. %) is designed based on the d-electrons theory, whose composition is adjusted to Md of 2.399 and Bo of 2.802 in Md-Bo map [29,30]. The alloy exhibits metastable characteristics and undergoes stress-induced  $\omega$  ( $\text{Si}\omega$ ) phase transformation during the dynamic compression. The stop rings are applied to control the compressive strains. Through optical microscopy (OM), X-ray diffraction (XRD), electron backscatter diffraction (EBSD), transmission electron microscopy (TEM) and differential scanning calorimetry (DSC) characterizations, the interaction between stress-induced structures and ASB is explored, and the complex microstructural evolution inside the matrix and ASB regions are revealed.

## 2. Material and method

The nominal composition of the designed alloy was Ti-6Mo-3.5Cr-1Zr (wt. %), whose  $\beta$  transus temperature was measured to be  $\sim 808$  °C through metallographic method. The ingot was cast via vacuum arc smelting for three times, and then it underwent homogenization at 1000 °C for 12 h, followed by a hot rolling at 740 °C with a deformation of 75%. Finally, the samples were solution-treated at 900 °C for 30 min and water quenched. All heat treatments were carried out under a high-purity argon atmosphere.

Dynamic compression tests at room temperature were performed on a Split Hopkinson Pressure Bar (SHPB) at a strain rate of  $\sim 3000$   $\text{s}^{-1}$ . The specimen with the size of  $\phi 5 \times 5$  mm was compressed to fracture to test its compressive strength and malleability. In addition, a series of stop rings were applied to control the maximum deformation of the specimen to explore the microstructural evolution under different compressive strains, as shown in the schematic diagram (Fig. 1). The material of the stop rings is C350 maraging steel with a high yield strength of  $\sim 1800$  MPa

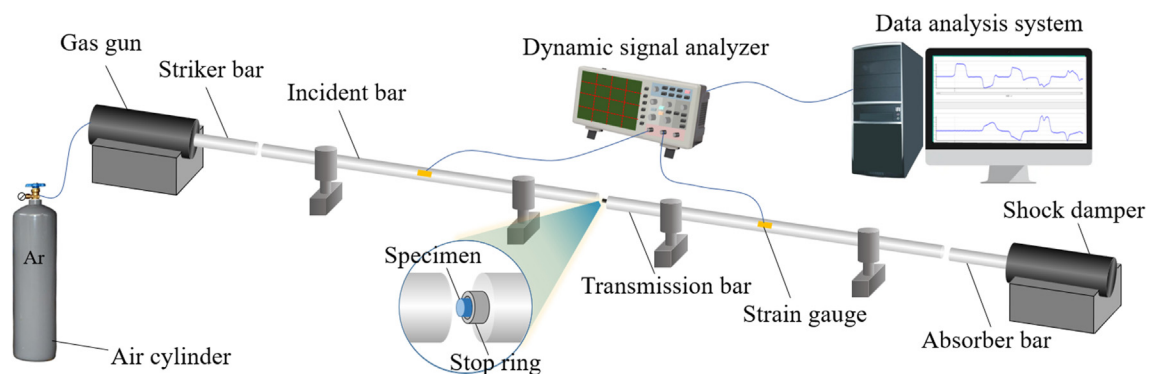
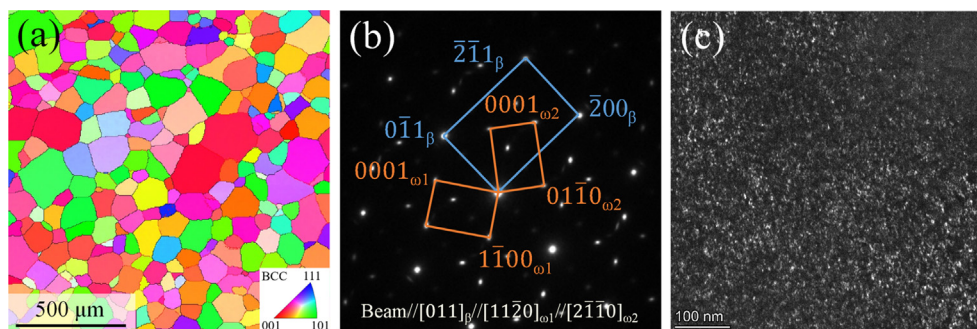


Fig. 1. Schematic diagram of dynamic compression experiment with stop rings.



**Fig. 2.** Microstructural analysis of the as-quenched Ti-6Mo-3.5Cr-1Zr alloy. (a) EBSD IPF map. (b) SAED pattern with beam//[011]<sub>β</sub>//[11 $\bar{2}$ 0]<sub>ω1</sub>//[1 $\bar{2}$ 10]<sub>ω2</sub>. (c) TEM DF image acquired using the ω reflection.

and a high hardness of  $\sim 57$  HRC, which can hardly be deformed under the loading conditions of this experiment. This material is also used as a stop ring in other reports [31,32]. The inner and outer diameters of the stop rings are 7 mm and 10 mm, respectively. The heights of the stop rings were processed to be 4.5 mm, 4 mm, 3.75 mm and 3.5 mm, which correspond to 10 %, 20 %, 25 % and 30 % deformations, respectively. Subsequently, the optical microscopy (OM), X-ray diffraction (XRD), electron backscatter diffraction (EBSD), and transmission electron microscopy (TEM) tests were performed on the specimen compressed to the specified strains.

The metallography analysis was carried out on optical microscopy (OM; LECO series Olympus PME-3). XRD were carried out using Bruker D8 Focus ( $\lambda_{\text{Cu}\alpha}$ : 0.154 nm, 2°/min, from 20°–90°). Rietveld refinement was performed using TOPAS 4.2 software to quantitatively calculate the relative content of each phase. Differential scanning calorimetry (DSC) test was carried out on NETZSCH DSC 404F3. EBSD maps were recorded under a voltage of 25 kV and current of 26  $\mu\text{A}$  on field emission scanning electron microscope (JSM 7200F). Prior to this process, the surface of specimen was mechanically polished, and then electrochemically polished in a  $\text{HClO}_4$ :  $\text{CH}_3(\text{CH}_2)_3\text{OH}$ : $\text{CH}_3\text{OH}$  (6:34:60) solution at 30 V, and  $-40$  °C. The scan area, step size and confidence index for the as-quenched state alloy were  $1.5 \text{ mm} \times 1.5 \text{ mm}$ ,  $5 \mu\text{m}$  and 0.33, respectively. While the three parameters for the 10 % strain state alloy were  $150 \mu\text{m} \times 150 \mu\text{m}$ ,  $0.25 \mu\text{m}$  and 0.18, respectively. EBSD data were analyzed by HKL's CHANNEL5 software. TEM were performed under a Talos F200X transmission electron microscope equipped with a 200 kV electron gun. High resolution TEM (HRTEM) obser-

vations have been made by using an aberration-corrected FEI Themis Z transmission electron microscope. The tested samples from the specimen's matrix area were prepared by ion thinning method, and that inside and near the ASB region were prepared following lift-out and plan-view methods [33] in a dual-beam focused ion beam (FIB) Helios Nanolab 600i (Thermo Fischer Scientific). TEM data were analyzed using Digital Micrograph (GMS 3, Gatan, Munich, Germany) software.

### 3. Results and discussion

#### 3.1. Microstructure and dynamic compression properties of the as-quenched alloy

As shown in the EBSD inverse pole figure (IPF) map (Fig. 2a), the as-quenched alloy is composed of equiaxed  $\beta$  grains with an average grain size of  $\sim 120 \mu\text{m}$ . A selected area electron diffraction (SAED) pattern taken along the  $[011]_{\beta}$  zone axis is presented in Fig. 2b, in addition to the  $\beta$  matrix, two variants of athermal  $\omega$  phases are also indexed. TEM dark-field (DF) image reveals that the precipitated nanoscale athermal  $\omega$  phases with grain sizes of  $1 \text{ nm} \sim 10 \text{ nm}$  are randomly dispersed inside the  $\beta$  matrix (Fig. 2c) [34,35].

The true stress–strain curves of the dynamically compressed specimens to 10%, 20%, 25%, 30% strain states and to fracture are shown in Fig. 3a, extremely high strain hardening trend can be observed. The compressive strength and malleability of the alloy are  $\sim 1152 \text{ MPa}$  and  $\sim 34 \%$ , respectively. The microstructure of

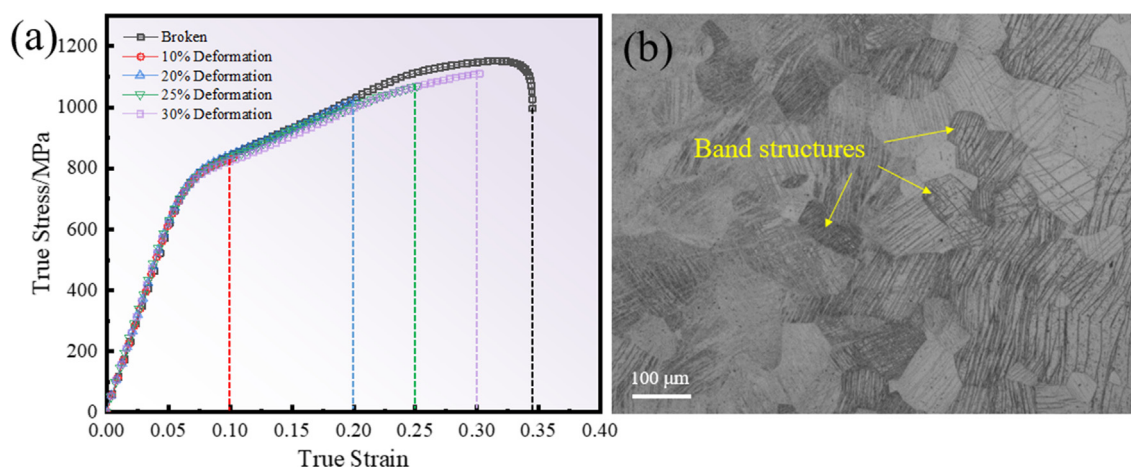


**Fig. 3.** The true stress–strain curves and microstructure after the dynamic compression. (a) The true stress–strain curves of the specimens dynamically compressed to broken and the 10%, 20%, 25% and 30% strain states. (b) The microstructure of the specimen compressed to fracture.

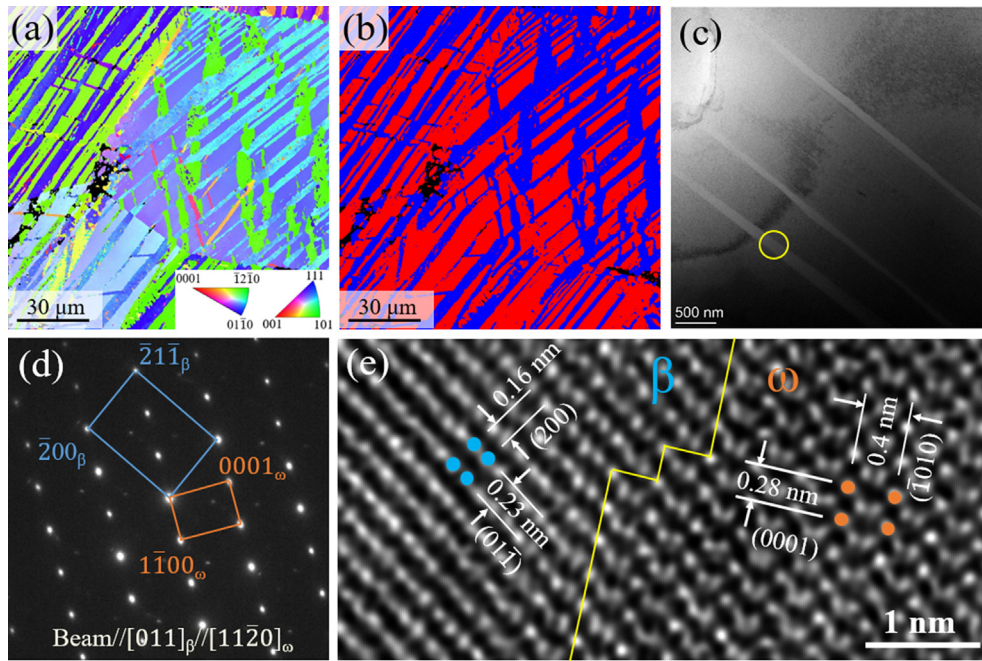


**Fig. 4.** EBSD and TEM analysis of the band structures. (a) EBSD IPF map. (b) EBSD Phase map. (c) TEM bright-field image. (d) SAED pattern recorded from the circled area in (c). (e) HRTEM image at  $\omega/\beta$  interface along  $[011]_{\beta}$  axis. The  $\omega$  and  $\beta$  phases are highlighted by orange and blue dots, respectively.

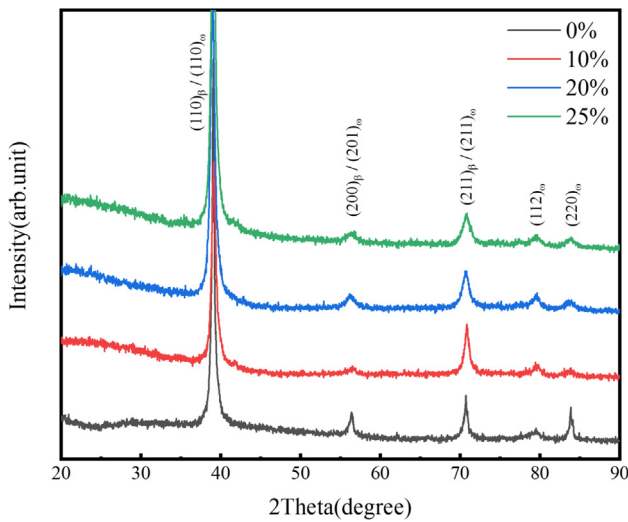


**Fig. 5.** XRD analysis of the alloy at 0%, 10%, 20% and 25% strain states.

the specimen compressed to failure is shown in Fig. 3b, in which a lot of band structures are found.

### 3.2. Analysis of the microstructural evolution during dynamic compression process

In order to gain an insight into the microstructural evolution during the dynamic compression, EBSD characterization was

performed. However, the sharpness resolution of the Kikuchi pattern would be significantly reduced by the high residual surface stress generated in the compressed specimens with high strain, hence, the low strain specimen of 10% strain is chosen for analysis. Its EBSD IPF map is shown in Fig. 4a, the bands with the width of  $3 \mu\text{m} \sim 10 \mu\text{m}$  run through the  $\beta$  grains and terminate at the grain boundaries. The bands structure can be found in the EBSD phase map (Fig. 4b), which are all hexagonal structure. These bands are generated from the body centered cubic (BCC)  $\beta$  matrix at relatively low strains, so the occurrence of stress-induced phase transformation can be inferred [8–10]. Further TEM SAED indicates that the stress-induced bands in Fig. 4c are the  $\omega$  phase (Fig. 4d). The high-resolution (HR) TEM image recorded from the  $[011]_{\beta}$  axis shows the atomic arrangement at  $\omega/\beta$  interface (Fig. 4e), in which the structural feature of the  $\omega$  phase and the  $\beta$  phase are highlighted by orange and blue dots, respectively. The interplanar distances of  $(01\bar{1})_{\beta}$ ,  $(200)_{\beta}$ ,  $(0001)_{\omega}$  and  $(\bar{1}010)_{\omega}$  are measured to be 0.23 nm, 0.16 nm, 0.28 nm and 0.4 nm, respectively. Based on the observations of SAED and HRTEM, the orientation relationship between the  $\omega$  and  $\beta$  phases is deduced as  $\{\bar{1}010\}_{\omega} // \{211\}_{\beta}$  and  $[11\bar{2}0]_{\omega} // [011]_{\beta}$ , which is consistent with the orientation relationship reported in Ti-36Nb-2.2Ta-3.7Zr-0.30 (at. %) alloy [36].

The phase analysis of the alloy under different strains are shown in Fig. 5. The alloy in each state is composed of  $\beta$  and  $\omega$  phases (the 0% state alloy contains only athermal  $\omega$  phase, while the alloy under 10%, 20% and 25% states contain athermal  $\omega$  phase and  $S\omega$  phase). Rietveld refinements were performed to obtain the relative contents of each phase [37]. The weighted profile R-factor

**Table 1**

The  $R_{\text{wp}}$  of Rietveld refinements, relative contents and lattice parameters of  $\beta$  and  $\omega$  phases under 0%, 10%, 20% and 25% strain states.

Deformation strain, %	$R_{\text{wp}}$ , %	$a/\text{\AA}$ ( $\beta/\omega$ )	$b/\text{\AA}$ ( $\beta/\omega$ )	$c/\text{\AA}$ ( $\beta/\omega$ )	wt, % ( $\beta/\omega$ )
0	7.95	3.261/4.489	3.261/4.489	3.261/2.840	69.3/30.7
10	8.56	3.264/4.587	3.264/4.587	3.264/2.833	54.7/45.3
20	6.96	3.262/4.584	3.262/4.584	3.262/2.832	40.8/59.2
25	7.63	3.265/4.569	3.265/4.569	3.265/2.849	33.5/66.5

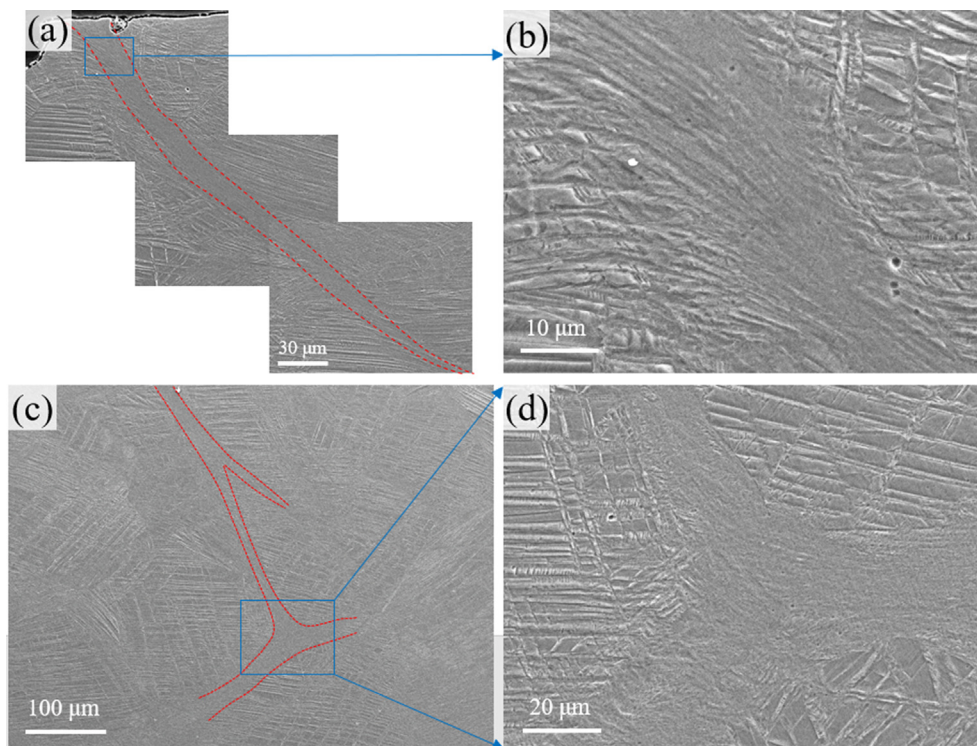


**Fig. 6.** SEM observation of the adiabatic shear band. (a) Overall morphology of adiabatic shear band. (b) Enlarged view for the boxed area in (a). (c) Bifurcation at the end of adiabatic shear band. (d) Enlarged view for the boxed area in (c).

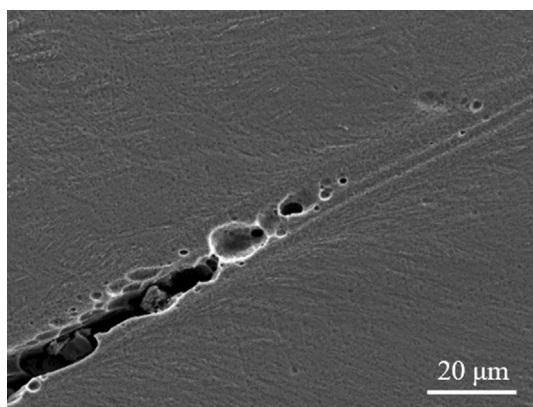


**Fig. 7.** SEM observation of the crack and micro-voids.

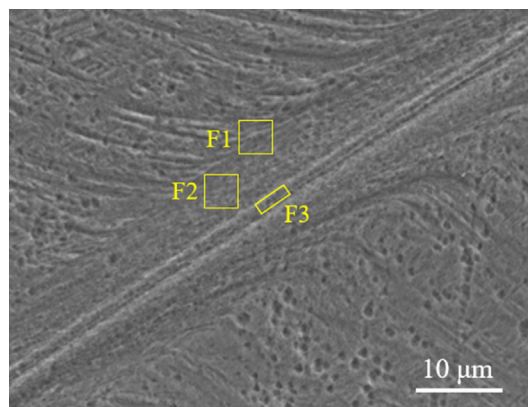


**Fig. 8.** The target zones in the adiabatic shear band region.

( $R_{wp}$ , %) of refinements, relative contents and lattice parameters of  $\beta$  and  $\omega$  phases under 0%, 10%, 20% and 25% strain states are shown in Table 1.

As the strain increases from 0% to 25%, the content of  $\omega$  phase increases from 30.7% to 66.5%, implying that the TRIP effect persists during plastic deformation. As the stress accumulates during the plastic deformation, the stress-induced phase transformation is activated in a growing number of original  $\beta$  grains. The continuous formation of  $Sl\omega$  bands interlace with each other in a net-like distribution, thus inducing the dynamic Hall-Petch effect [38]. The flow stress increment  $\Delta\sigma_1$  contribution from the  $Sl\omega$  bands is given by [39]:

$$\Delta\sigma_1 = nMGb/\Lambda \tag{1}$$

where  $n$  is the maximum number of dislocations accumulated at grain boundaries on a specific slip plane,  $M$  is the Taylor factor;  $G$

is the alloy shear modulus,  $b$  is the magnitude of the Burgers vector,  $\Lambda$  represents the dislocation mean free path, which is mainly determined by the mean spacing between the bands.

The phase interface of  $\beta/Sl\omega$  can play the similar role of grain boundaries strengthening. The dislocation mean free path is reduced due to a motion hindering effect by the  $\beta/Sl\omega$  interface, which eventually results in strain hardening of the material.

### 3.3. Analysis of adiabatic shear band and crack in samples with 30 % strain

The formation of ASB is observed in samples with 30 % strain. The direction of the ASB is 45° from the compressive direction (Fig. 6a), and the  $Sl\omega$  bands on both sides of ASB deform along the shear direction (Fig. 6b). In addition, the ASB in Fig. 6c-d tends

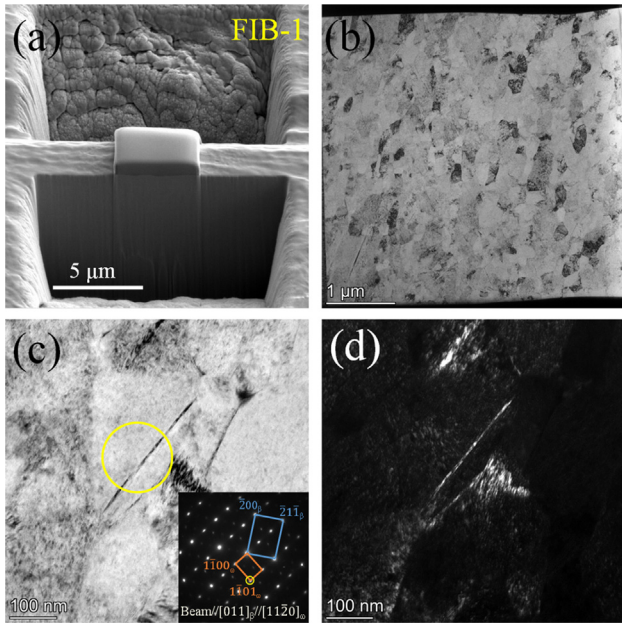


**Fig. 9.** TEM analysis of the outer edge of adiabatic shear band. (a) FIB sample prepared by lift-out method. (b) TEM BF image showing the grain size. (c) TEM BF image showing the band structures (the inset shows the SAED pattern obtained from the circled area). (d) TEM DF image corresponding to the band structures based on the  $[1\ 1\ 0]_{\alpha}$  reflection in the inset of (c).

to get around the stress-induced bands region and propagate along the original  $\beta$  grains boundaries, which results in a bifurcation at the end. This reflects the hindering effect on the ASB expansion by the stress-induced structures. These obstacles in the formation and expansion of the ASB results in a relatively high malleability of the alloy.

Crack formation is also observed under this state (Fig. 7). Lots of micro-voids are observed near the crack tip. This crack feature is

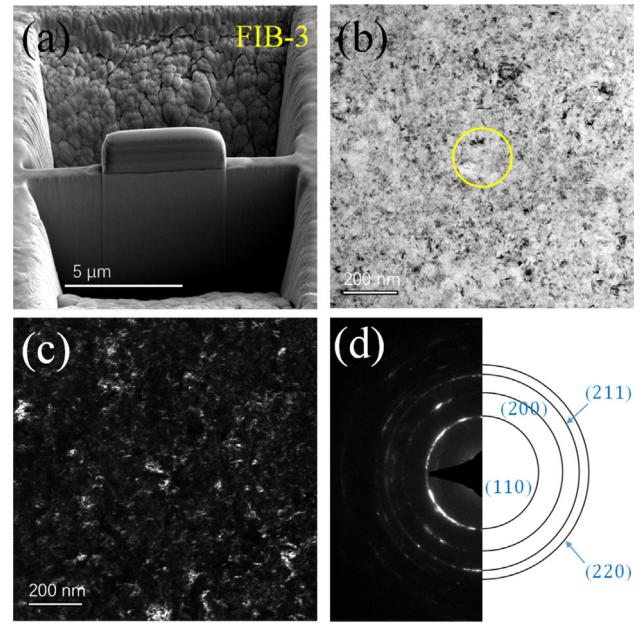


**Fig. 11.** TEM analysis of the center zone in adiabatic shear band. (a) FIB sample prepared by plan-view method. (b) TEM BF image. (c) TEM DF image. (d) SAED pattern obtained from the circled area in (b).

similar to that observed in pure Ti [40] and  $\alpha/\beta$  dual phase titanium alloys [41–43]. A reasonable inference is that micro-voids are first generated in the adiabatic shear band, and their interconnection and expansion lead to the formation of macroscopic cracks.

### 3.4. Microstructural analysis of the adiabatic shear band region

It is well known that the failure of titanium alloys under dynamic compression first occurs at the ASB region, and the failure of the ASB is dominated by its microstructure. In order to explore

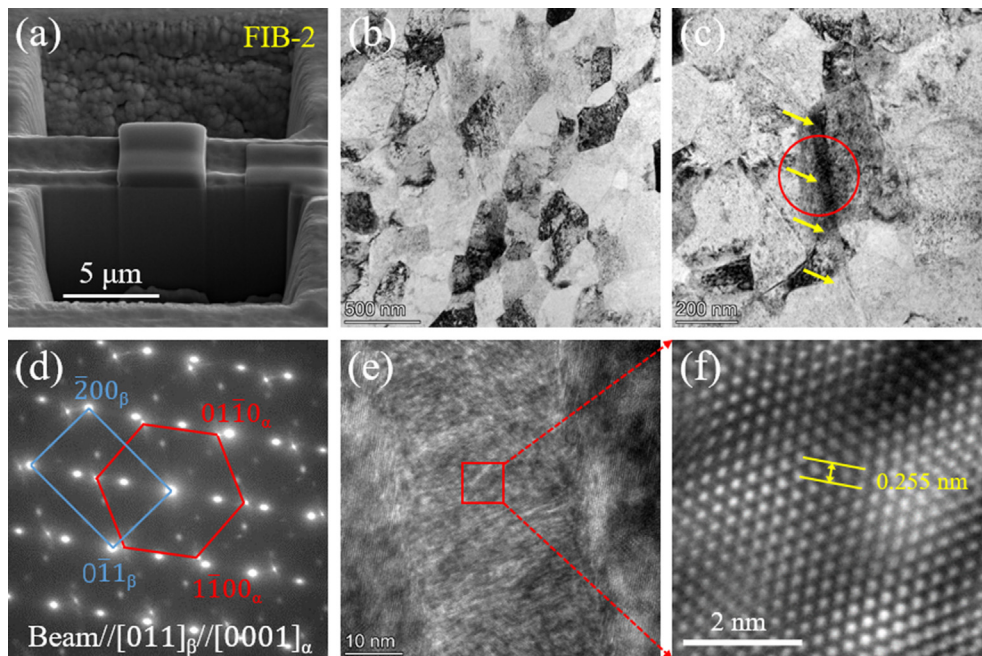


**Fig. 10.** TEM analysis of the transition zone in adiabatic shear band. (a) FIB sample prepared by lift-out method. (b) TEM BF image showing the grain size. (c) TEM BF image showing the band structure. (d) SAED pattern obtained from the circled area in (c). (e) HRTEM image of the band area. (f) The inverse FFT filtered HRTEM image of the band area.

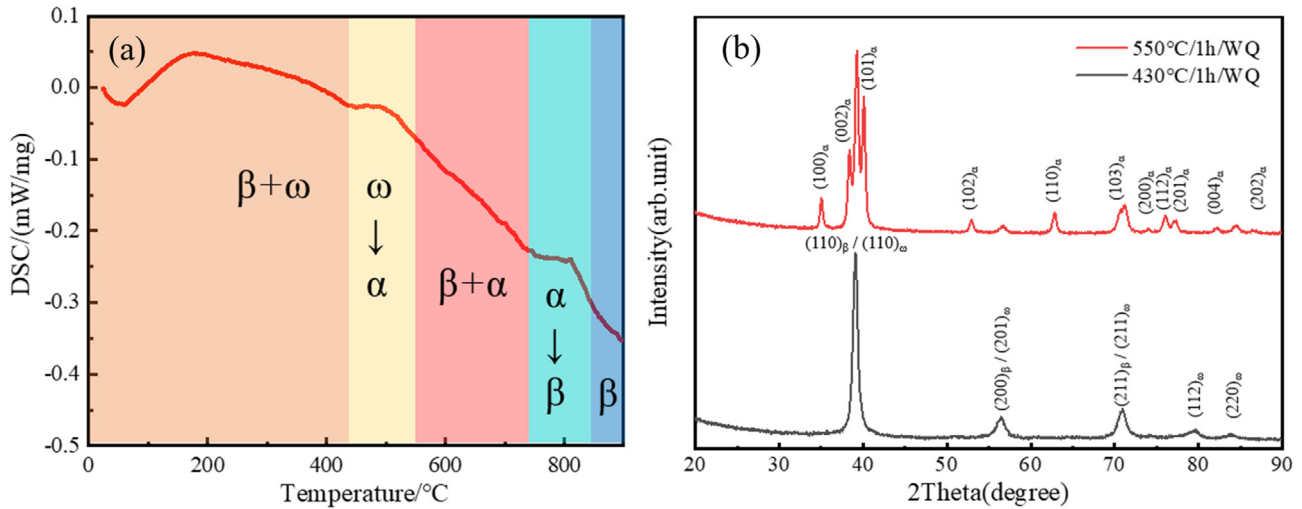


**Fig. 12.** Temperature analysis of phase transformation among  $\omega$ ,  $\alpha$ , and  $\beta$  phases. (a) DSC exothermic curve. (b) XRD analysis of two heat treatment states: 430°C/1h/WQ and 550°C/1h/WQ.

the microstructural evolution in ASB region, three typical zones including the outer edge (F1), the transition zone (F2) and the center (F3) of the ASB are selected for TEM analysis (Fig. 8).

TEM observations on the outer edge of ASB (F1 zone in Fig. 8) are shown in Fig. 9. Lift-out method is used to prepare FIB sample in the target zone (Fig. 9a). The microstructure of this zone is consisted of deformed ultrafine grains and dynamic recrystallization grains [44–46], whose average grain size is significantly refined to  $\sim 500$  nm (Fig. 9b). In addition, a small amount of band structure is observed (Fig. 9c), which is confirmed as  $Si\omega$  phase by the SAED (inset of Fig. 9c) and TEM DF image (Fig. 9d).

TEM observations on the transition zone of ASB (F2 zone in Fig. 8) are shown in Fig. 10. Lift-out method is used to prepare FIB sample in the target zone (Fig. 10a). The average grain size in F2 zone is  $\sim 300$  nm (Fig. 10b). Band structures are also detected in this zone (Fig. 10c), which are confirmed as the hexagonal close packed (HCP) structure by SAED (Fig. 10d). The HRTEM image and corresponding inverse fast Fourier transform (FFT) filtered image of the band area are shown in Fig. 10e and Fig. 10f, respectively. The

interplanar distances of  $(01\bar{1}0)$  is measured to be  $\sim 0.255$  nm, which indicates that the band structure is  $\alpha$  phase generated by recrystallization.

TEM observations on the center of ASB (F3 zone in Fig. 8) are shown in Fig. 11. Plan-view method is used to prepare FIB sample in the target zone (Fig. 11a). The TEM BF and DF images show that the average grain size in this zone is less than 10 nm (Fig. 11b–c). SAED pattern determines its structure as single  $\beta$  nanograins (Fig. 11d).

In summary, the average grain size decreases from the outer edge to the center of the ASB, which indicates an increment of the degree of dynamic recrystallization along this path. In addition, the microstructural evolution of  $(\beta + \omega) \rightarrow (\beta + \alpha) \rightarrow (\beta)$  from the outer edge to the transition zone and then to the center of the ASB is observed. DSC is performed using the sample after dynamic compression (including  $\beta$  and  $\omega$  phases) to explore the mechanism of microstructural evolution, as shown in Fig. 12a. The slope of DSC exothermic curve changes abruptly in the two ranges of 430 °C  $\sim$  550 °C and 740 °C  $\sim$  840 °C, which indicates the occur-

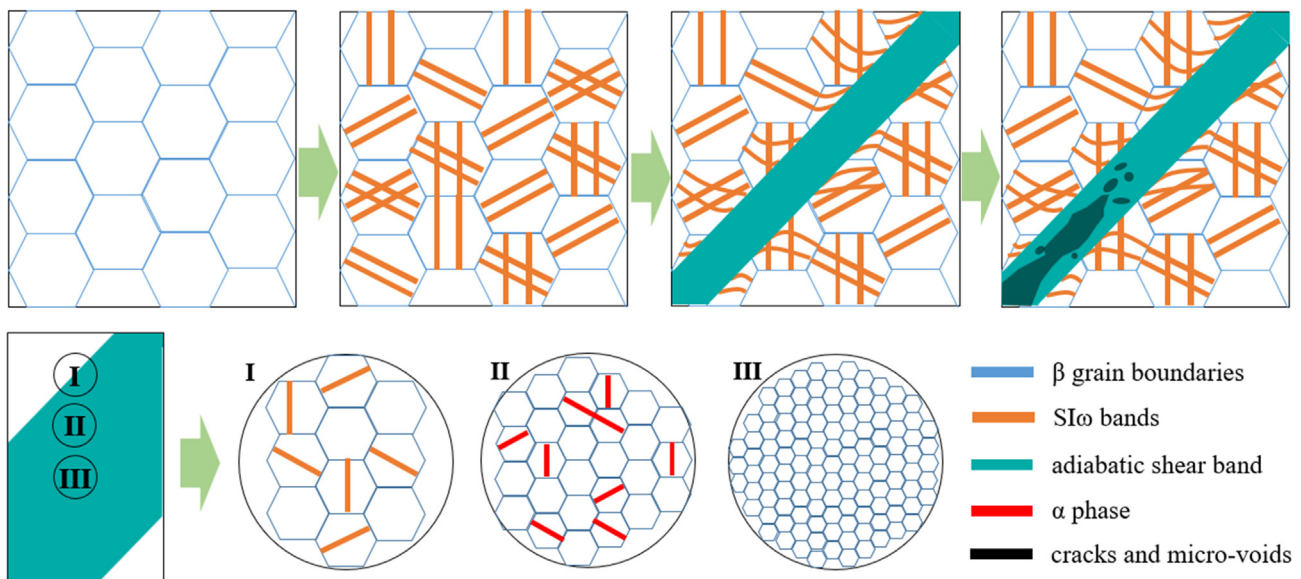


**Fig. 13.** Schematic diagram of microstructural evolution and failure process of the Ti-6Mo-3.5Cr-1Zr alloy during dynamic compression.

rence of phase transformation [47,48]. The samples after dynamic compression are heat treated at 430 °C and 550 °C respectively for 1 h and then water quenched (WQ) to room temperature for XRD analysis, as shown in Fig. 12b. The microstructure is composed of ( $\beta + \omega$ ) phases after aging at 430°C and ( $\beta + \alpha$ ) phases after aging at 550°C. This proves that the  $\omega \rightarrow \alpha$  phase transformation takes place between 430 °C ~ 550 °C, which is consistent with the DSC results. Therefore, it can be concluded that the local temperature in the transition zone of ASB exceeds 430 °C. On the other hand, the phase transformation in the range of 740 °C ~ 840 °C corresponds to the  $\alpha \rightarrow \beta$ . The existence of the single  $\beta$  phase in center zone of ASB proves that the local temperature exceeds the  $\beta$  transus temperature (~808 °C). This phenomenon is consistent with the internal temperature variation of the adiabatic shear band calculated by Zhou through crystal plastic finite element method [49].

Based on the above analysis, the microstructural evolution and failure process of the alloy during dynamic compression are schematically shown in Fig. 13. The metastable  $\beta$  phase undergoes a stress-induced phase transformation under the action of compressive stress. The stress-induced  $\omega$  bands shorten the dislocation mean free path and thus increase the flow stress of the alloy. In addition, the bands are observed to hinder the formation and expansion of ASB. The grains in ASB are substantially refined. The microstructural evolution of ( $\beta + \omega$ ) $\rightarrow$ ( $\beta + \alpha$ ) $\rightarrow$ ( $\beta$ ) occurs along the outer edge  $\rightarrow$  transition zone  $\rightarrow$  centre of ASB region. Furthermore, numerous micro-voids are generated inside ASB, which is believed to result from a combination of the thermal softening and microstructural softening (dynamic recrystallization) [50–53]. The connection and expansion of these micro-voids form cracks and lead to failure of the material.

#### 4. Conclusion

In this work, a metastable  $\beta$  titanium alloy Ti-6Mo-3.5Cr-1Zr is innovatively designed using d-electrons theory. The stress-induced microstructural evolution and adiabatic shearing behavior of the alloy under dynamic compression are investigated. The conclusions are as follows:

- (1) The compressive stress–strain curve of the alloy shows a strain hardening trend with the compressive strength up to ~ 1152 MPa. The strain hardening of the alloy is attributed to the occurrence of stress-induced  $\omega$  ( $S\omega$ ) phase transformation. XRD showed that the content of  $\omega$  phase increases from 30.7% to 66.5% with the strain varies from 0% to 25%.
- (2) The  $S\omega$  bands hinder the formation and propagation of adiabatic shear bands (ASB), which delays the failure of the alloy. The alloy therefore exhibits a high compressive fracture strain of ~ 34%.
- (3) Compared with the matrix, the average grain size in the ASB region is gradually refined due to the dynamic recrystallization. Nanograins with grain size less than 10 nm are detected in the center of ASB. In addition, the microstructural evolution along outer edge  $\rightarrow$  transition zone  $\rightarrow$  center of the ASB region is ( $\beta + \omega$ ) $\rightarrow$ ( $\beta + \alpha$ ) $\rightarrow$ ( $\beta$ ), which is confirmed to be caused by the temperature increasement in ASB.

#### Declaration of Competing Interest

The authors declare that they have no known competing financial interests or personal relationships that could have appeared to influence the work reported in this paper.

#### Acknowledgements

The authors are grateful to the financial support from the Natural Science Foundation of China (Grant No. 52101005) and Natural Science Foundation of China (Grant No. 51901102).

#### References

- [1] S.S. Sidhu, H. Singh, M.A. Gepreel, A review on alloy design, biological response, and strengthening of  $\beta$ -titanium alloys as biomaterials, *Mater. Sci. Eng. C* 121 (2021), <https://doi.org/10.1016/j.msec.2020.111661> 111661.
- [2] A. Gupta, R. Khatirkar, J. Singh, A review of microstructure and texture evolution during plastic deformation and heat treatment of  $\beta$ -Ti alloys, *J. Alloys Compd.* 899 (2022), <https://doi.org/10.1016/j.jallcom.2021.163242> 163242.
- [3] Q. Zhao, Q. Sun, S. Xin, Y. Chen, C. Wu, H. Wang, J. Xu, M. Wan, W. Zeng, Y. Zhao, High-strength titanium alloys for aerospace engineering applications: A review on melting-forging process, *Mater. Sci. Eng. A* 845 (2022), <https://doi.org/10.1016/j.msea.2022.143260> 143260.
- [4] W. Weng, A. Biesiekierski, Y. Li, C. Wen, Effects of selected metallic and interstitial elements on the microstructure and mechanical properties of beta titanium alloys for orthopedic applications, *Materialia* 6 (2019), <https://doi.org/10.1016/j.mtla.2019.100323> 100323.
- [5] M. Kaur, K. Singh, Review on titanium and titanium based alloys as biomaterials for orthopaedic applications, *Mater. Sci. Eng. C* 102 (2019) 844–862, <https://doi.org/10.1016/j.msec.2019.04.064>.
- [6] D. Cai, X. Zhao, L. Yang, R. Wang, G. Qin, D.-f. Chen, E. Zhang, E. Zhang, A novel biomedical titanium alloy with high antibacterial property and low elastic modulus, *J. Mater. Sci. Technol.* 81 (2021) 13–25.
- [7] M. Morinaga, N. Yukawa, H. Adachi, Theory of the d Electrons Alloy Design, *J. Iron and Steel Inst.* 71 (1985) 1441–1451, [https://doi.org/10.2355/tetsutohagane1955.71.11\\_1441](https://doi.org/10.2355/tetsutohagane1955.71.11_1441).
- [8] M. Marteleur, F. Sun, T. Gloriant, P. Vermaut, P.J. Jacques, F. Prima, On the design of new  $\beta$ -metastable titanium alloys with improved work hardening rate thanks to simultaneous TRIP and TWIP effects, *Scr. Mater.* 66 (2012) 749–752, <https://doi.org/10.1016/j.scriptamat.2012.01.049>.
- [9] F. Sun, J.Y. Zhang, M. Marteleur, C. Brozek, E.F. Rauch, M. Veron, P. Vermaut, P.J. Jacques, F. Prima, A new titanium alloy with a combination of high strength, high strain hardening and improved ductility, *Scr. Mater.* 94 (2015) 17–20.
- [10] Y. Fu, W. Xiao, D. Kent, M.S. Dargusch, J. Wang, X. Zhao, C. Ma, Ultrahigh strain hardening in a transformation-induced plasticity and twinning-induced plasticity titanium alloy, *Scr. Mater.* 187 (2020) 285–290, <https://doi.org/10.1016/j.scriptamat.2020.06.029>.
- [11] L. Ren, W. Xiao, D. Kent, M. Wan, C. Ma, L. Zhou, Simultaneously enhanced strength and ductility in a metastable  $\beta$ -Ti alloy by stress-induced hierarchical twin structure, *Scr. Mater.* 184 (2020) 6–11, <https://doi.org/10.1016/j.scriptamat.2020.03.039>.
- [12] M.A. Meyers, G. Subhash, B.K. Kad, L. Prasad, Evolution of microstructure and shear-band formation in  $\alpha$ -hcp titanium, *Mech. Mater.* 17 (1994) 175–193, [https://doi.org/10.1016/0167-6636\(94\)90058-2](https://doi.org/10.1016/0167-6636(94)90058-2).
- [13] B. Dodd, Y. Bai, Adiabatic Shear Localization: *Frontiers and Advances*, Elsevier, 2012.
- [14] M.A. Meyers, H. Pak, Observation of an adiabatic shear band in titanium by high-voltage transmission electron microscopy, *Acta Metall.* 34 (1986) 2493–2499, [https://doi.org/10.1016/0001-6160\(86\)90152-5](https://doi.org/10.1016/0001-6160(86)90152-5).
- [15] Y. Guo, Q. Ruan, S. Zhu, Q. Wei, J. Lu, B. Hu, X. Wu, Y. Li, Dynamic failure of titanium: Temperature rise and adiabatic shear band formation, *J. Mech. Phys. Solids* 135 (2020), <https://doi.org/10.1016/j.jmps.2019.103811> 103811.
- [16] Y. Guo, Q. Ruan, S. Zhu, Q. Wei, H. Chen, J. Lu, B. Hu, X. Wu, Y. Li, D. Fang, Temperature rise associated with adiabatic shear band: causality clarified, *Phys. Rev. Lett.* 122 (2019), <https://doi.org/10.1103/PhysRevLett.122.015503> 015503.
- [17] X. Liu, Y. Zhou, X. Zhu, D. Wang, Q. Fan, The failure mechanism at adiabatic shear bands of titanium alloy: High-precision survey using precession electron diffraction and geometrically necessary dislocation density calculation, *Mater. Sci. Eng. A* 746 (2019) 322–331, <https://doi.org/10.1016/j.msea.2019.01.016>.
- [18] J.L. Sun, P.W. Trimby, F.K. Yan, X.Z. Liao, N.R. Tao, J.T. Wang, Shear banding in commercial pure titanium deformed by dynamic compression, *Acta Mater.* 79 (2014) 47–58, <https://doi.org/10.1016/j.actamat.2014.07.011>.
- [19] Y. Yang, X.M. Li, X.L. Tong, Q.M. Zhang, C.Y. Xu, Effects of microstructure on the adiabatic shearing behaviors of titanium alloy, *Mater. Sci. Eng. A* 528 (2011) 3130–3133, <https://doi.org/10.1016/j.msea.2010.12.068>.
- [20] X. Liu, C. Tan, J. Zhang, F. Wang, H. Cai, Correlation of adiabatic shearing behavior with fracture in Ti-6Al-4V alloys with different microstructures, *Int. J. Impact Eng.* 36 (2009) 1143–1149, <https://doi.org/10.1016/j.ijimpeng.2008.12.007>.
- [21] H. Yang, D. Wang, X. Zhu, Q. Fan, Dynamic compression-induced twins and martensite and their combined effects on the adiabatic shear behavior in a Ti-8.5Cr-1.5Sn alloy, *Mater. Sci. Eng. A* 759 (2019) 203–209, <https://doi.org/10.1016/j.msea.2019.05.040>.
- [22] C. Brozek, F. Sun, P. Vermaut, Y. Millet, A. Lenain, D. Embury, P.J. Jacques, F. Prima, A  $\beta$ -titanium alloy with extra high strain-hardening rate: Design and mechanical properties, *Scr. Mater.* 114 (2016) 60–64.
- [23] J.F. Xiao, Z.H. Nie, C.W. Tan, G. Zhou, R. Chen, M.R. Li, X.D. Yu, X.C. Zhao, S.X. Hui, W.J. Ye, Y.T. Lee, The dynamic response of the metastable  $\beta$  titanium alloy

- Ti-2Al-9.2Mo-2Fe at ambient temperature, *Mater. Sci. Eng. A* 751, *Mater. Sci. Eng.*, A 751 (2019) 191–200.
- [24] J. Peirs, W. Tirry, B. Amin-Ahmadi, F. Coghe, P. Verleysen, L. Rabet, D. Schryvers, J. Degrieck, Microstructure of adiabatic shear bands in Ti6Al4V, *Mater. Sci. Eng. A* 75 (2013) 79–92.
- [25] Y. Jiang, Z. Chen, C. Zhan, T. Chen, R. Wang, C. Liu, Adiabatic shear localization in pure titanium deformed by dynamic loading: Microstructure and microtexture characteristic, *Mater. Sci. Eng. A* 640 (2015) 436–442, <https://doi.org/10.1016/j.msea.2015.06.028>.
- [26] G. Sukumar, B.B. Singh, A. Bhattacharjee, K.S. Kumar, A.K. Gogia, Ballistic impact behaviour of  $\beta$ -CEZ Ti alloy against 7.62 mm armour piercing projectiles, *Int. J. Impact Eng.* 54 (2013) 149–160, <https://doi.org/10.1016/j.ijimpeng.2012.11.002>.
- [27] X. Xu, L. Wang, D.H. Zhao, W.W. Du, Dynamic Behavior in Ti-5553 Alloy with  $\beta$  Phase under Compression Loading, *Appl. Mech. Mater.* 782 (2015) 88–96, <https://doi.org/10.4028/www.scientific.net/AMM.782.88>.
- [28] X. Zhu, Q. Fan, D. Wang, H. Gong, Y. Gao, J. Yuan, K. Chen, F. Qian, Influence of twins found in adiabatic shear bands on dynamic recrystallization of a near  $\beta$  Ti-5.5Mo-7.2Al-4.5Zr-2.65Nb-2.1Cr alloy, *Scr. Mater.* 842 (2022), <https://doi.org/10.1016/j.msea.2022.143084> 143084.
- [29] D. Kuroda, M. Niinomi, M. Morinaga, Y. Kato, T. Yashiro, Design and mechanical properties of new  $\beta$  type titanium alloys for implant materials, *Mater. Sci. Eng. A* 243 243 (1-2) (1998) 244–249.
- [30] M. Abdel-Hady, K. Hinoshita, M. Morinaga, General approach to phase stability and elastic properties of  $\beta$ -type Ti-alloys using electronic parameters, *Scr. Mater.* 55 (2006) 477–480, <https://doi.org/10.1016/j.scriptamat.2006.04.022>.
- [31] A. Bhattacharyya, G. Ravichandran, D. Rittel, Strain rate effect on the evolution of deformation texture for  $\alpha$ -Fe, *Metall. Mater. Trans. A* 37 (2006) 1137–1145, <https://doi.org/10.1007/s11661-006-1092-9>.
- [32] M. Vural, G. Ravichandran, D. Rittel, Large strain mechanical behavior of 1018 cold-rolled steel over a wide range of strain rates, *Metall. Mater. Trans. A* 34 (2003) 2873–2885, <https://doi.org/10.1007/s11661-003-0188-8>.
- [33] N.S. Rajput, K. Sloyan, D.H. Anjum, M. Chiesa, A.A. Ghaferi, A user-friendly FIB lift-out technique to prepare plan-view TEM sample of 2D thin film materials, *Ultramicroscopy* 235 (2022), <https://doi.org/10.1016/j.ultramic.2022.113496> 113496.
- [34] Y. Ohmori, T. Ogo, K. Nakai, S. Kobayashi, Effects of  $\omega$ -phase precipitation on  $\beta \rightarrow \alpha$ ,  $\alpha'$  transformations in a metastable  $\beta$  titanium alloy, *Mater. Sci. Eng. A* 312 (2001) 182–188, [https://doi.org/10.1016/S0921-5093\(00\)01891-8](https://doi.org/10.1016/S0921-5093(00)01891-8).
- [35] M. Li, X. Min, K. Yao, F. Ye, Novel insight into the formation of  $\alpha'$ -martensite and  $\omega$ -phase with cluster structure in metastable Ti-Mo alloys, *Acta Mater.* 164 (2018) 322–333, <https://doi.org/10.1016/j.actamat.2018.10.048>.
- [36] Y.B. Wang, Y.H. Zhao, Q. Lian, X.Z. Liao, R.Z. Valiev, S.P. Ringer, Y.T. Zhu, E.J. Lavernia, Grain size and reversible beta-to-omega phase transformation in a Ti alloy, *Scr. Mater.* 63 (2010) 613–616, <https://doi.org/10.1016/j.scriptamat.2010.05.045>.
- [37] R.W. Cheary, A.A. Coelho, J.P. Cline, Fundamental Parameters Line Profile Fitting in Laboratory Diffractometers, *J. Res. Natl. Inst. Stand. Technol.* 109 (2004) 1–25, <https://doi.org/10.6028/jres.109.002>.
- [38] K. Yao, X. Min, Static and dynamic Hall-Petch relations in {332}<113> TWIP Ti-15Mo alloy, *Mater. Sci. Eng. A* 827 (2019), <https://doi.org/10.1016/j.msea.2021.142044> 142044.
- [39] O. Bouaziz, S. Allain, C. Scott, Effect of grain and twin boundaries on the hardening mechanisms of twinning-induced plasticity steels, *Scr. Mater.* 58 (2008) 484–487, <https://doi.org/10.1016/j.scriptamat.2007.10.050>.
- [40] Y. Guo, R. Liu, A. Arab, Q. Zhou, B. Guo, Y. Ren, W. Chen, C. Ran, P. Chen, *Mater. Sci. Eng. A* 833 (2022) 142340.
- [41] P. Landau, S. Osovski, A. Venkert, V. Gärtnerová, D. Rittel, The genesis of adiabatic shear bands, *Sci. Rep.* 6 (2016) 37226, <https://doi.org/10.1038/srep37226>.
- [42] I. Mendoza, D. Villalobos, B.T. Alexandrov, Crack propagation of Ti alloy via adiabatic shear bands, *Mater. Sci. Eng. A* 645 (2015) 306–310, <https://doi.org/10.1016/j.msea.2015.08.035>.
- [43] Y. Du, X. Yang, Z. Li, F. Hao, Y. Mao, S. Li, X. Liu, Y. Feng, Z. Yan, Shear localization behavior in hat-shaped specimen of near- $\alpha$  Ti-6Al-2Zr-1Mo-1V titanium alloy loaded at high strain rate, *T. Nonferr. Metal. Soc.* 31 (2021) 1641–1655, [https://doi.org/10.1016/S1003-6326\(21\)65604-2](https://doi.org/10.1016/S1003-6326(21)65604-2).
- [44] S. Liu, Y.Z. Guo, Z.L. Pan, X.Z. Liao, E.J. Lavernia, Y.T. Zhu, Q.M. Wei, Y. Zhao, Microstructural softening induced adiabatic shear banding in Ti-23Nb-0.7Ta-2Zr-O gum metal, *J. Mater. Sci. Technol.* 54 (2020) 31–39, <https://doi.org/10.1016/j.jmst.2020.03.042>.
- [45] S. He, W. Zeng, R. Jia, J. Xu, X. Zhang, The mechanical response and failure mechanism of a near  $\alpha$  titanium alloy under high-strain-rate compression at different temperatures, *Mater. Sci. Eng. A* 814 (2021), <https://doi.org/10.1016/j.msea.2021.140749> 140749.
- [46] K. Sun, X. Yu, C. Tan, H. Ma, F. Wang, H. Cai, Influence of adiabatic shear bands intersection on the ballistic impact of Ti-6Al-4V alloys with three microstructures, *Mater. Sci. Eng. A* 606 (2014) 257–267, <https://doi.org/10.1016/j.msea.2014.03.091>.
- [47] H. Shahmir, T.G. Langdon, Characteristics of the allotropic phase transformation in titanium processed by high-pressure torsion using different rotation speeds, *Mater. Sci. Eng. A* 667 (2016) 293–299, <https://doi.org/10.1016/j.msea.2016.05.001>.
- [48] J.M. Chaves, O. Florêncio, P.S.S. Jr, P.W.B. Marques, C.R.M. Afonso, Influence of phase transformations on dynamical elastic modulus and anelasticity of beta Ti-Nb-Fe alloys for biomedical applications, *J. Mech. Behav. Biomed.* 46 (2015) 184–196, <https://doi.org/10.1016/j.jmbbm.2015.02.030>.
- [49] Y. Zhou, Q. Fan, X. Liu, D. Wang, X. Zhu, K. Chen, Multi-scale crystal plasticity finite element simulations of the microstructural evolution and formation mechanism of adiabatic shear bands in dual-phase Ti20C alloy under complex dynamic loading, *J. Mater. Sci. Tech.* 59 (2020) 138–148, <https://doi.org/10.1016/j.jmst.2020.03.079>.
- [50] P. Longère, Respective/combined roles of thermal softening and dynamic recrystallization in adiabatic shear banding initiation, *Mech. Mater.* 117 (2018) 81–90, <https://doi.org/10.1016/j.mechmat.2017.10.003>.
- [51] S. Osovski, D. Rittel, P. Landau, A. Venkert, Microstructural effects on adiabatic shear band formation, *Scr. Mater.* 66 (2012) 9–12, <https://doi.org/10.1016/j.scriptamat.2011.09.014>.
- [52] J.A. Rodríguez-Martínez, G. Vadillo, D. Rittel, R. Zaera, J. Fernández-Sáez, Dynamic recrystallization and adiabatic shear localization, *Mech. Mater.* 81 (2015) 41–45, <https://doi.org/10.1016/j.mechmat.2014.10.001>.
- [53] S. Osovski, D. Rittel, A. Venkert, The respective influence of microstructural and thermal softening on adiabatic shear localization, *Mech. Mater.* 56 (2013) 11–12, <https://doi.org/10.1016/j.mechmat.2012.09.008>.